Revision 1

Crystal Structure of Guinier-Preston Zones in Orthopyroxene: Z-contrast imaging and *ab inito* study

Huifang Xu [*1, 2], Zhizhang Shen [1], Hiromi Konishi [1], and Gufeng Luo [3]

[1] NASA Astrobiology Institute, Department of Geoscience,
University of Wisconsin - Madison
Madison, Wisconsin 53706

[2] Material Science Program,
University of Wisconsin-Madison,
Madison, Wisconsin 53706

[3] Department of Geoscience,
Nanjing University,
Nanjing, China 210008

* Corresponding author: Dr. Huifang Xu

Tel: 1-608-265-5887

Fax: 1-608-262-0693

Email: hfxu@geology.wisc.edu

Abstract

Nano-precipitates of Guinier-Preston zones (or G. P. zones) occur in slowly cooled orthopyroxenes (OPX). Due to their nanometer sizes and intergrowth with host OPX, both X-ray diffraction and high-resolution TEM imaging cannot provide a consistent structure model for the G. P. zone precipitates. Combining Z-contrast imaging and density functional theory (DFT) methods, a correct crystal structure for the G. P. zone precipitates can be obtained, because Z-contrast imaging can reveal positions and occupancies of atoms directly. The crystal structure for the G. P. zone has $P2_1/c$ symmetry with 4 types of tetrahedral chains (OA1, OA2, OB, OC). The structure can be considered as periodic stacking of half unit cells of enstatite sub-layers and of diopside sub-layers in a twinning-like relationship along ***a***-axis. The G. P. zones that precipitate out from their host Ca-bearing OPX at low temperature are metastable with respect to end members of enstatite and diopside.

Keywords: orthopyroxene, diopside, G. P. zone, nano mineral, DFT, Z-contrast imaging, order-disorder, enstatite

Introduction

Guinier-Preston Zones (or G. P. zones) in orthopyroxenes (OPX) are nanometer scale precipitates with composition between OPX and diopside (Di) (Champness and Lorimer, 1973, 1974; Buseck et al., 1980; Nord, 1980; Takeda et al., 1982; Smyth and Swope, 1990; Heinemann et al., 2000). The plate-like precipitates have thickness of one to several unit cells along *a*-axis (Nord, 1980; Takeda et al., 1982; Langenhorst et al., 2012). It was proposed that the OPX crystals with G. P. zones are products of extremely slow cooling of their host rocks, especially those with multi-layer G. P. zones in extraterrestrial rocks (Nord, 1980; Takeda et al., 1982; Smyth and Swope, 1990).

It was proposed that multi-layer G. P. zones (i.e., several unit cells wide along ***a***-axis) have structure with $Pbc2_1$ symmetry (Nord, 1980; Buseck et al., 1980). The structure consists of two half-unit cell layers (or, sub-layers) of diopside (Di) and enstatite (En) with ideal stoichiometry of $CaMgSi_2O_6 \cdot (Mg,Fe)_2Si_2O_6$, or, $Ca(Mg,Fe)_3(Si_2O_6)_2$. Ca atoms are ordered in octahedral strips with opposite skews (Nord, 1980). However, Smyth and Swope (1990) proposed $P2_1/c$ symmetry for G. P. zones with Ca atoms in octahedral trips with same skews within diopsode-like sub-layers. Reported unit cell parameters for the Mg-rich G. P. zones are: a=18.40 Å, b=8.83 Å, c =5.18 Å, and $\beta = 90.0°$ (Smyth and Swope, 1990). A recent study indicates that the Ca atoms are disordered in diopside sub-layers based on high-resolution TEM (HRTEM) images (Langenhorst et al., 2006). The crystal structure for the G. P. zones in OPX still remains controversial.

We report new results from Z-contrast images of an OPX with G. P. zones, and a crystal structure model for multi-layer G. P. zones based on observed cation positions and *ab-initio* calculation using density function theory (DFT) methodology. Scanning transmission electron microscopy (STEM) uses a high-angle annular dark-field (HAADF) detector to give the most highly localized 1s Bloch state imaging, which eliminates most of the obvious effects of dynamical diffraction (Kirkland, 1998; Pennycook, 2002). Z-contrast images are HAADF images with atomic resolution. Multiple diffraction effects that appear in high-resolution transmission electron microscopic (HRTEM) imaging can be eliminated or minimized in Z-contrast imaging, because Z-contrast imaging uses non-coherent elastically scattered electrons at high scattering angle (Fig. 1A). Using a HAADF detector and annular bright-field (ABF) detector, both a Z-contrast image and an annular bright-field image can be obtained simultaneously (Fig. 1). Bright spots in the Z-contrast image correspond to positions of atom columns. The contrast is roughly reversed in ABF image (Fig. 1B, 1C). The intensity of Z-contrast images is dependent on the atomic number of atom and occupancy in the site through $\mathbf{Z^n}$ (Kirkland, 1998; Pennycook, 2002). The power **n** depends on experimental conditions. For the instrument used to acquire our images (FEI Titan 80-200 aberration corrected scanning/transmission electron microscope), n values are 1.70, 1.97, 2.27, and 2.15 for camera lengths of 77 mm, 128 mm, 160 mm, and 196 mm, respectively (Shi, 2013). Local composition and occupancy may be obtained from measured intensities. We can obtain positions of atoms directly over a large range of thickness, with Z-contrast to help distinguish columns of different atoms and their occupancies along the beam direction.

Sample and Experimental Methods

Orthopyroxene megacrysts were collected from a norite pegmatite in Black Hill of Chengde, Hebei Province, North China. The OPX appears brown in color with (100) parting. The reported chemical formula for the OPX is:

$(Ca_{0.068}Mg_{1.102}Fe_{0.812}Mn_{0.019}Ti_{0.008}Al_{0.042})(Si_{1.920}, Al_{0.080})O_6$.

It can also be expressed as $En_{56}Fs_{41}Wo_3$ (Luo et al., 1988, 1992). Unit cell parameters for OPX are: a = 18.310Å, b = 8.900Å , c = 5.223Å. A double-side polished thin section normal to ***c***-axis cutting was prepared. Fresh OPX areas were mounted on TEM Cu grids and ion milled. The ion milled TEM sample was thinly coated with carbon.

TEM and STEM studies were carried out using a FEI Titan 80-200 aberration corrected scanning/transmission electron microscope operated at 200 kV coupled with an EDAX high resolution EDS detector and Gatan image filtering system. This instrument can image single atoms with ~ 0.1 nm or better spatial resolution in STEM mode. Probe current was set at 24.5 pA. All Z-contrast images were acquired using a condition of camera length of 160 mm, in order to maximize the difference among different atoms. Intensity (I) from an atom column is proportional to $Z^{2.27}$ for the image acquisition condition (Shi, 2013). Atomic number (Z) of Si, Fe and Mg are 4, 26 and 12, respectively. Intensity at Si site is $I \sim 14^{2.27}$. Intensity at an M site occupied by x Fe and (1-x) Mg is $I \sim [x\ 26^{2.27} + (1\text{-}x)12^{2.27}]$. Occupancies of Fe and Mg in individual M1 and M2 sites (columns along ***c***-axis) can be calculated based on their relative intensities with respect to neighboring Si sites (columns). Average occupancy is obtained by measuring occupancies of multiple sites.

The code VASP was used for DFT calculations (Kresse et al., 1996). The general gradient approximation (GGA) with the Perdew, Burke, and Ernzerhof (PBE) parameters was employed for the exchange correlation functional (Perdew et al., 1996). The projector augmented wave (PAW) method with an energy cutoff of 600 eV was used for calculation. Monkhorst-Pack meshes of 4×2×1, 4×2×1, and 2×2×2 were found to be sufficient for the structures of enstatite, G. P.-zones, and diopside, respectively. All DFT calculations are performed at 0K for Fe-free end-members.

Results and Discussions

Electron Diffraction and Z-contrast Imaging

Selected-area electron diffraction (SAED) from the OPX with G. P. zones shows diffraction streaks along ***a**** direction and weak diffraction spots that violate *a*-glide in OPX (Fig. 2). This is very similar to the diffraction pattern from a lunar OPX with multi-layer G. P. zones reported by Nord (1980). The weak diffraction spots (odd *h*) are slightly off center from two neighboring strong diffraction spots with even *h*, especially the high-order diffraction spots. For instance, the position of the (11 00) weak spot is slightly off center between strong diffraction spots of (10 00) and (12 00) (Fig. 2). The weak diffraction spots (odd) are not from host OPX, but from multi-layer G. P. zones. Unit cell dimensions for multi-layer G. P. zones along ***a***-axis are slightly larger than the host OPX. Unit cell dimensions along ***b***-axis and ***c***-axis are about same as those of the host OPX. Measured unit cell parameters for multi-layer G.P. zones are: a = 18.35 (±0.02) Å, b = 8.90 (±0.02) Å, c = 5.22 (±0.02) Å.

A low-magnification STEM bright-filed (BF) image and HAADF image show G. P. zones (Fig. 3). The contrast of G. P. zones is better in the HAADF image (Z-contrast image) than in the ABF image, because Z-contrast images are sensitive to chemical composition. An outlined area in the Z-contrast image contains a G. P. zone with a 3-layer repetition layers, that is 3 x 18.35 Å. A fast Fourier transform (FFT) pattern from an area without G. P. zones only shows spots that obey the *a*-glide absences perpendicular to *c*-axis and the 2-fold screw axis along the ***b***-axis due to even *0k0* reflections (Fig. 4A). However, the FFT pattern from the outlined area with a multi-layer G. P. zone shows extra weak spots (e.g., 100, 700) that violate *a*-glide absences perpendicular to the ***c***-axis (Fig. 4B). High magnification Z-contrast imaging (Fig. 5B) clearly shows positions of M1 sites with low intensity and M2 sites with high intensity in the host OPX, because Fe atoms preferentially occupy M2 sites. Based on intensities from columns of Si, M1 and M2 sites, M1 sites are dominated by Mg (~92% Mg and ~8% Fe), and M2 sites are dominated by Fe (~ 80% Fe and 20% Mg). Uncertainty for the occupancies is about 3%. The FFT pattern from the Z-contrast image does not show odd *0k0* spots (Fig. 5D), however, the FFT pattern from the ABF image (Fig. 5A) clearly shows odd *0k0* spots (Fig. 5C) due to multiple diffraction of low-angle scattered electrons. For an OPX with bulk composition of $En_{56}Fs_{41}Wo_3$, if the entire Wo component is combined with some amount of En component from diopside sub-layers in the G. P. zones, the remaining OPX will have a composition of $En_{56}Fs_{44}$. The intensity profile for M1 and M2 sites shows much stronger intensity in M2 sites than in M1 sites (Fig. 6A), because M2 sites are dominated by Fe (Z=26) and M1 sites are dominated by Mg (Z=12). However, the intensity difference in the diopside sub-layer of the G. P. zone is much smaller than that in the host OPX (Fig. 6B), because M2 sites are occupied by Ca (Z=20) and M1 sites in the G.P. zones are very similar to M1 sites in the host and dominated by Mg (Z=12). The

147 intensity profile across the diopside sub-layer shows that the Ca-Mg sub-layer has lower
148 intensity than that in the host OPX (Fig. 6C). The Z-contrast image support early models of
149 diopside-like sub-layer in the G.P. zone that were proposed by Nord (1980) and Smyth and
150 Swope (1990).

151

152 The image also shows the difference between OA and OB chains in OPX (Fig. 7). The
153 difference is in their tetrahedral chain angle that is the angle between bridge oxygen in O_3- O_3-
154 O_3. The angle in OA chains is close to 180° degrees (160° ~ 170°) while the angle in OB chains
155 is close to 120° degrees (135° ~ 145°) (Cameron and Papike, 1980). If we view the structure
156 along ***c***-axis, the bridge oxygen atoms approximately overlap in OA chains, and not overlap in
157 OB chains (see the overlaid structure model of OPX at low-left corner of Fig. 7). The bridge
158 oxygen atoms in OB chains will be approximately overlapping with Si atoms. In [001]-zone axis
159 Z-contrast images, the OA chains will display "V"-like contrast while OB chains will display
160 dumbbell-like contrast (Fig. 7). The structure model of OPX can be overlaid on the image based
161 on positions of OA and OB chains. The skews of octahedral layers (++-- for OPX, and ++ for
162 diopside) (Cameron and Papike, 1980) can be determined in the Z-contrast image if we can
163 identify OA and OB chains. The distances between neighboring M2 sites (Ca atoms) in the
164 diopside sub-layer of a G. P. zone are ~3.7 Å, and ~5.1 Å, respectively. The distances between
165 neighboring M2 sites in the OPX are ~4.2 Å, and ~4.7 Å, respectively (Fig. 6). The Z-contrast
166 image clearly shows ordering of Ca atoms within the (100) sub-layer of the G. P. zone. The
167 octahedral strips for the Ca-Mg atoms will have the same skew direction (i.e., either ++, or --),
168 instead of opposite skews in a previously hypothesized structure model proposed by Nord (1980).

Previously reported Ca-Mg disordering in diopside-like sub-layers (Langenhorst et al., 2006) could be an artifact of the strong dynamic effect in HRTEM imaging mode. HRTEM images are phase contrast images, and not sensitive to chemical composition.

The tetrahedral chains between two Ca-Mg layers or in diopside sub-layers are not OB-like chains (with smaller tetrahedral chain angle), but are OA-like chains (with large tetrahedral chain angle). We label them as OC chains because they are in OB chain positions of the host OPX, but more like OA chains regarding their bridge oxygen atoms (i.e., "V"-like appearance in Z-contrast image). There are two types of chains in OPX with *Pbca* symmetry. However, at least three different types of chains are evident in the Z-contrast images: chains in enstatite sub-layer, chains in diopside sub-layer, and chains between enstatite sub-layer diopside sub-layer (Fig. 7). Previously proposed G.P. zone structures have 4 types of chains (Nord, 1980; Smyth and Swope, 1990). The observed positions for Ca, Mg, and Fe, and different types of chains can test structure model of the G.P. zone.

DFT Calculation:

An initial crystal structure model for multi-layer G. P. zone was constructed based on OPX structure and the observed positions of Ca atoms and differences in tetrahedral chains. Structure model with *P1* symmetry and chains in enstatite structure was used as initial input, although we do not know exact rotation angles for the chains. The final calculated structure with lowest energy has $\boldsymbol{P2_1/c}$ symmetry that is consist with a model proposed by Smyth and Swope (1990). The calculated structure has 4 types of chains, although the OA1 and OA2 chains between diopside-sublayer and enstatite sub-layer have similar rotation angles (Fig. 8). In order

to compare the energy of two end members and to evaluate the accuracy of calculations for pyroxene, enstatite and diopside structures were also calculated. The volumes of unit cells calculated for enstatite and diopside shrink by 1~2% compared to experimentally measured data. This is because the calculations were done at 0K while the experimental samples, to which they are compared, were quenched at 323K (Cameron et al., 1973; and Carlson et al., 1988). The *a* and *c* lattice parameters of the calculated G. P. zones match quite well with those of the experimental values, although the calculated structures are unconstrained by host OPX. The calculated unit cell volume of Fe-free G. P. zones is slightly larger than reported by Smyth and Swope (1990) (Table 2). The host enstatite with a slightly smaller unit cell will confine the lattice of the G. P. zone precipitates due to coherent and semi-coherent interfaces between the G. P. zone precipitates and the host enstatite.

The calculated crystal structure for multi-layer G. P. zone has 4 types of tetrahedral chains (Figs. 8-10). OB chains (O3-O3-O3=133.58˚) are similar to OB chains in OPX (Figs. 8, 10). There are 2 types of OA chains (OA1: O3-O3-O3=158.24˚ and OA2: O3-O3-O3=145.91˚) between the Ca-Mg octahedral layer and Fe-Mg-octahedral layer (Figs. 8, 10). OC chains (O3-O3-O3=151.52˚) between Ca-Mg-octahedral layers are very similar to OA chains in OPX. The space group of a calculated G. P. zone is determined to be $P2_1/c$. The β angle is very close to 90° (Table 2).

Discussion regarding a G. P. zone with $Pbc2_1$ symmetry and OPX with $P2_1ca$ symmetry

An OPX with G. P. zones will display weak diffraction spots that violate *a*-glide and *b*-glide planes in [001] and [100] zone-axis diffraction patterns of the OPX, respectively. Nord (1980) proposed a symmetry for the G. P. zone precipitates based on weak diffraction spots in violation of *a*-glide only. According to this model, Ca atoms will be in octahedral bands with opposite skews similar to Mg in proto-enstatite (Nord, 1980, Buseck et al., 1980). This type of structure will be unstable for large cations of Ca (Cameron, and Papike, 1970).

The reported OPX with $\boldsymbol{P2_1ca}$ symmetry contains G. P. zones (Smyth, 1974; Steel, 1975; Evensen et al., 1979; Harlow et al., 1979; Smyth and Swope, 1990). The studied sample also shows diffraction violating *b*-glide perpendicular to $\boldsymbol{a}$-axis (Luo et al., 1988, 1992). The presence of G. P. zones with $\boldsymbol{P2_1/c}$ symmetry explains the observed diffraction spots that violate *b*-glide in reported OPX and extra diffraction spots that violate *a*-glide from the G. P. zones with $\boldsymbol{P2_1/c}$ symmetry (Smyth, 1974; Smyth and Swope, 1990). Because G. P. zones are very thin nano-plates parallel to (100) of the host OPX, it is very difficult to recognize them in [100] zone-axis TEM images. The weak diffraction spots and streaking that violate *a*- and *b*-glide plans are considered resulting from G. P. zones instead of OPX. Smyth and Swope (1990) provided detailed explanations.

OPX with G. P. zones indicates slow cooling of its host rock (Nord, 1980; Smyth and Swope, 1990). The nano-precipitates of G. P. zones are intermediary or transition phases between both the structures and compositions of the host OPX and a thermodynamically stable precipitate of diopside (Champness and Lorimer, 1973; Nord, 1980). The structure of a G. P. zone can be considered as the combination of a one-half enstatite unit cell and a unit cell of

diopside, i.e. G. P. = $\frac{1}{2}$ En + Di. The energy of the right side (i.e., $\frac{1}{2}$ En + Di) is lower (~0.18 eV per $MSiO_3$) than that of a G. P. zone. The G. P. zones are metastable nano-phases with respect end-members of diopside and enstatite. Precipitation of the G. P. zones may lower interfacial energy between the precipitates and the host OPX. Figure 11 schematically illustrates the variations of free energies in a diopside-enstatite binary system. At low temperature, coherent precipitation of G. P. zones within OPX may have lower energy than coherent precipitation of diopside (CPX) within OXP due to lattice mis-fit in their ***a***-dimensions. However, the energy is higher than a mechanical mixture of thermodynamically stable phases of OPX and diopside.

Implications

Because Z-contrast imaging can provide information about both positions and occupancies of atom columns, an intracrystalline Fe-Mg distribution coefficient (K_d) between the M1 (Fe/Mg=8/92) and M2 (Fe/Mg=80/20) sites can be obtained. OPX with a low distribution coefficient (~0.02) corresponds to a structural state at an apparent temperature of ~ 250°C to 350 °C based on the published relationship between the intracrystalline Fe-Mg distribution coefficient and equilibrium temperature (Molin et al., 1991; Zema et al., 1999; Heinemann et al., 2000; Stimpfl et al., 2005; Wang et al., 2005). The low apparent equilibrium temperature is related to extremely slow cooling of the host rock (Heinemann et al., 2008).

It was reported that OPX with G. P. zones has larger activation energy for Fe-Mg disordering at high temperature than an OPX with the same composition but without G. P. zones (Heinemann et al., 2000). Ordered Ca atoms in diopside-like sub-layers may inhibit Fe diffusion into M1 sites and even Ca sites. Uniform distribution of G. P. zones may slow down Fe-Mg

disordering in host OPX. The combination of Z-contrast imaging and DFT methods may be used for determining occupancies of atoms in crystallographic sites of minerals with solid solutions as well as solving crystal structures of other natural nano-precipitates and nano-minerals.

The original meaning of G. P. zones refers to nano-precipitates with intermediate structure and composition between 2 end-members in metal alloys (see detail description in Buseck et al., 1980). The G. P. zones in OPX are very similar to mixed-layer clay minerals, such as interstratified chlorite/serpentine minerals (Banfield and Bailey, 1996; Xu and Veblen, 1996). The observed G. P. zones in the enstatite - diopsiode system may also be described as nano-precipitates of interstratified enstatite / diopside, although OA1 and OA2 chains between enstatite sub-layer and diopside sub-layer are new and different.

ACKNOWLDEGEMENTS

This work is supported by NASA Astrobiology Institute (N07-5489) and NSF (EAR-095800, MRI). Authors thank Prof. Izabela Szlufarska of University of Wisconsin for the help in DFT calculation. Authors than Dr. Jun Wu and an anomynous reviewer for critical reviews and helpful suggestions.

References

Banfield, J.F., and Bailey, S.W. (1996) Formation of regularly interstratified serpentine – chlorite minerals by tetrahedral inversion in long-period serpentine polytypes. American Mineralogist, 81, 79-81.

Buseck, P. R., Nord, G. L., and Veblen, D. R. (1980) Subsolidus phenomena in pyroxenes. In Charles T. Prewitt ed. "Pyroxenes". Reviews in Mineralogy, Vol. 7, page117-211.

Cameron, M., Sueno, S., Prewitt, C.T., and Papike, J.J. (1973) High-temperature crystal chemistry of acmite, diopside, hedenbergite, jadeite, spodumene and ureyite, 58, 594-618.

Cameron, M., and Papike, J.J. (1970) Crystal chemistry of silicate pyroxenes. Reviews in Mineralogy, Vol. 7, page 5-92.

Carlson, W.D., Swinnea, J.S., and Miser, D.E. (1998) Stability of orthoenstatite at high temperature and low pressure. American Mineralogist, 73, 1255-1263

Champness, P.E., and Lorimer, G.W., (1973) Precipitation (exsolution) in an orthopyroxene. Journal of Material Science, 8, 467–474.

Champness, P.E. and Lorimer, G.W. (1974) A direct lattice-resolution study of precipitation (exsolution) in orthopyroxene. Phil. Mag., 30, 357-365.

Evensen, N.M., Hamilton, P.J., Harlow, G.E., Klimentidis, R., O'Nion, R.K., and Prinz, M. (1979) Silicate inclusions in Weekeroo station: planetary differentiates in an iron meteorite. Lunar and Planetary Science, X, 376-377.

Harlow, G.E., Nehru, C.E., Prinz, M., Taylor, G.J., and Keil, K. (1979) Pyroxene in Serra de Mage: History in comparison with Moama and Moor County. Earth and Planetary Science Letters, 43, 173-181.

Heinemann, R., Kroll, H., Langenhorst, F., and Lueder, T. (2000) Time and temperature variation of the intracrystalline Fe^{2+}, Mg fractionation in Johnstown meteoritic orthopyroxene. European Journal of Mineralogy, 12, 163-176.

Heinemann, R., Kroll, H., and Langenhorst, F. (2008) Relationship between Guinier-Preston zones and the kinetics of the intracrystalline Fe^{2+}, Mg exchange reaction in Johnstown meteoritic orthopyroxene. European Journal of Mineralogy, v. 20, 551-561.

Kirkland, E.J. (2010) Advanced computing in electron microscopy. Plenum Press, New York, 250 pp.

Kresse, G., and Furthmüller, J. (1996) Efficiency of ab-initio total energy calculations for metals and semiconductors using a plane-wave basis set. Computational Materials Science, 1, 15-50.

Langenhorst, F., Smyth, J.R., and H. Kroll, H. (2006) On the nature of Guinier-Preston zones in meteoritic and lunar orthopyroxene. Lunar and Planetary Science, XXXVII, 2104.

Luo, G., Xu, H. F., Xue, J., Hu, M., Fan, C., and Zhang, S. (1988) The first discovery of terrestrial orthopyroxene with space group $P2_1ca$. Kexue Tongbao (Science Bulletin, China), 33, 1552-1554.

Luo, G., Xue, J., Xu, H.W., Xu, H. F., and Hu, M. (1992) Confirmation of the terrestrial occurrence of orthopyroxene with space group $P2_1ca$. American Mineralogist, 77, 115-120.

Molin G. M., Saxena S. K., and Brizi E. (1991) Iron-magnesium order-disorder in an orthopyroxene crystal from the Johnstown meteorite. Earth Planet. Sci. Lett., 105, 260 – 265.

Nord, G. L. (1980) The composition, structure, and stability of guinier-preston zones in lunar and terrestrial orthopyroxene. Physics and Chemistry of Minerals, 6: 109 - 128

Pennycook, S. (2002) Structure determination through Z-contrast microscopy. Advances in imaging and electron physics, 173-206 .

Perdew, J.P., Burke, K., and Ernzerhof, M. (1996) Generalized gradient approximation made simple. Physical Review Letters, 18, 3865-3868.

Shi, F. (2013) Advanced electron microscopy of novel ferromagnetic materials and ferromagnet / oxide interfaces in magnetic tunnel junctions. Ph. D. Dissertation, University of Wisconsin - Madison.

Smyth, J. R. (1974) Low orthopyroxene from a lunar deep crustal rock: a new pyroxene polymorph of space group $P2_1ca$. Geophyical Research Letters, 1, 27-29.

Smyth J.R., and Swope R.J. (1990) The origin of space group violations in a lunar orthopyroxene. Phys. Chem. Min., 17, 438-443.

Steele, I.M. (1975) Mineralogy of lunar norite 78235: second lunar occurrence of $P2_1ca$ pyroxene from Apollo 17 soils. American Mineralogist, 60, 1086-1091.

Stimpfl, M., Ganguly, J., and Molin, G. M. (2005) Kinetics of Fe^{2+} – Mg order-disorder in orthopyroxene: experimental studies and applications to cooling rates of rocks. Contrib Mineral Petrol, 150, 319-334.

Takeda, H., Mori, H., and Miyamoto, M. (1982) Comparison of thermal history of orthopyroxenes between Lunar Norites 78236, 72255, and diogenites. Proceedings of the Thirteenth Lunar and Planetary Science Conference, Part 1**.** Journal of Geophysical Research, 87, supplement, p. A124-A130.

Wang, L., Moon, N, Zhang Y., Dunham, W. R., and Essene, E. J. (2005) Fe-Mg order-disorder in orthopyroxenes. Geochimica et Cosmochimica Acta, 69, 5777–5788.

Xu, H, and Veblen, DR (1996) Interstratification and other reaction microstructures in the chlorite-berthierine series. Contribution to Mineralogy and Petrology, 124, 291-301.

Zema, M., Domeneghetti, M. C., and Tazzoli, V. (1999) Order-disorder kinetics in orthopyroxene with exsolution products. American Mineralogist, 84, 1895–1901.

Figure captions

Figure 1: (A) Schematic diagram of STEM showing formation of a Z-contrast image (or HAADF image) and annular bright-field (ABF) image. ABF image (B) and Z-contrast image (C) of magnetite (Fe_3O_4) showing position of Fe atom columns. ABF image also shows positions of oxygen atom columns (B). Structure model of magnetite along [110] zone-axis is also inserted in both images for comparison.

Figure 2: SAED pattern from OPX with G. P. zones showing streaking and very weak diffraction spots that violate *a*-glide.

Figure 3: Low magnification ABF STEM image (A) and Z-contrast image (B) showing G. P. zones with relatively lower intensity with respect to host OPX (B). An outlined area shows a 3-layer G. P. zone. The intensity changes from top-left to low-right indicate specimen thickness changes (from thin at top-left to thick in low-right).

Figure 4: FFT patterns from Z-contrast image without G. P. zones (A) and with a 3-layer G. P. zone (B). Some extra spots violating *a*-glide appear (arrowed). No odd *0k0* spots appear in either FFT pattern.

Figure 5: High magnification ABF STEM image (A) and Z-contrast image (B) of OPX with G. P. zones (relatively low intensity). Layers labeled with G. P. are the positions of the diopside sub-layers. FFT patterns from the BF STEM image show even and odd *0k0* spots, whereas FFT patterns from the Z-contrast image show even *0k0* spots only.

Figure 6: Line profiles of intensities along line a (OPX host), line b (diopside sub-layer), and across the diopside sub-layer zone area outlined in Figure 5B. Notice the differences in distance between neighboring M2 sites, ~ 4.2 Å for Fe atoms in the OPX, and ~ 3.7 Å for Ca atoms in the diopside sub-layer.

Figure 7: Z-contrast image containing a G. P. zone with projections of the OPX structure and G. P. zone structure along [001] zone-axis. OA and OB tetrahedral chains are can be identified in the OPX host based on their appearance as "V" or dumbbell-like shapes.

Figure 8: Structure models of OPX (with *Pbca* symmetry and a G. P. zone with $P2_1/c$ symmetry projected along ***c***-axis). OC chains are between Ca-Mg bands in the diopside sub-layer.

Figure 9: Structure models of OPX (with *Pbca* symmetry and a G. P. zone with $P2_1/c$ symmetry projected along ***b***-axis). OC chains are in the diopside sub-layer. Two Ca-Mg polyhedral bands in the diopside sub-layer have the same skew.

Figure 10: Diagrams showing rotations and angles between bridge oxygen atoms (O3-O3-O3) of the 4 types of tetrahedral chains in the structure of a G. P. zone. The O3-O3-O3 angles in tetrahedral chains are 151.52˚ for OC chains, 133.58˚ for OB chains, 158.24˚ for OA1 chains, and 145.91˚ for OA2 chains, respectively.

Figure 11: Diagram which schematically illustrates free energies for OPX (*Pbca*), CPX ($C2_1/c$), CPX ($C2_1/c$) within OPX, and a G. P. zone within OPX. The energy for coherent intergrowth of OPX and a G. P. zone is lower than the coherent intergrowth of OPX and CPX, although it is higher than the energy of equilibrium phases of OPX and CPX (lower red curve).

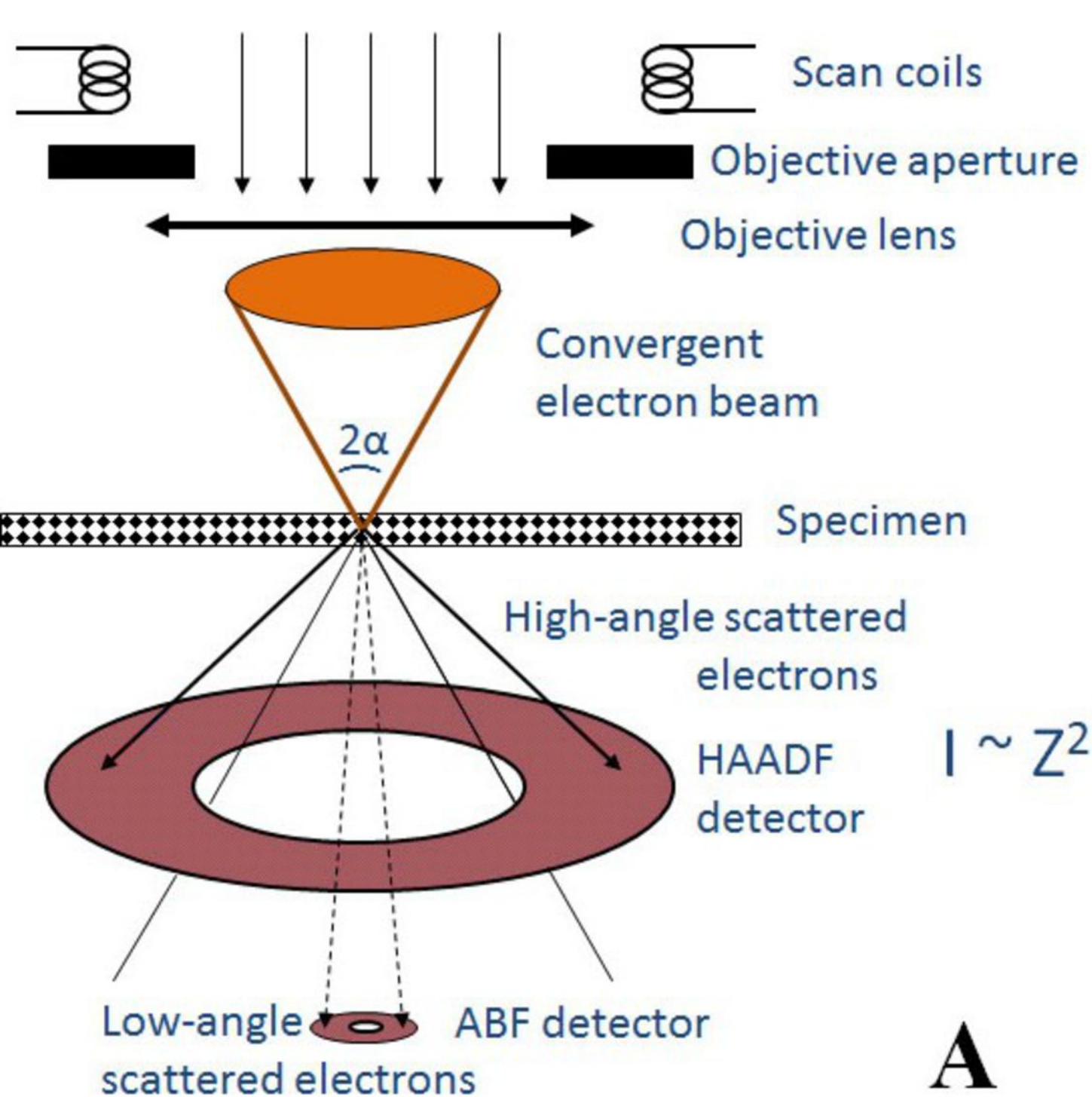
Scan coils
Objective aperture
Objective lens
Convergent
electron beam
2α
Specimen
High-angle scattered
electrons
HAADF
detector
Low-angle
scattered electrons
ABF detector

$I \sim Z^2$

A

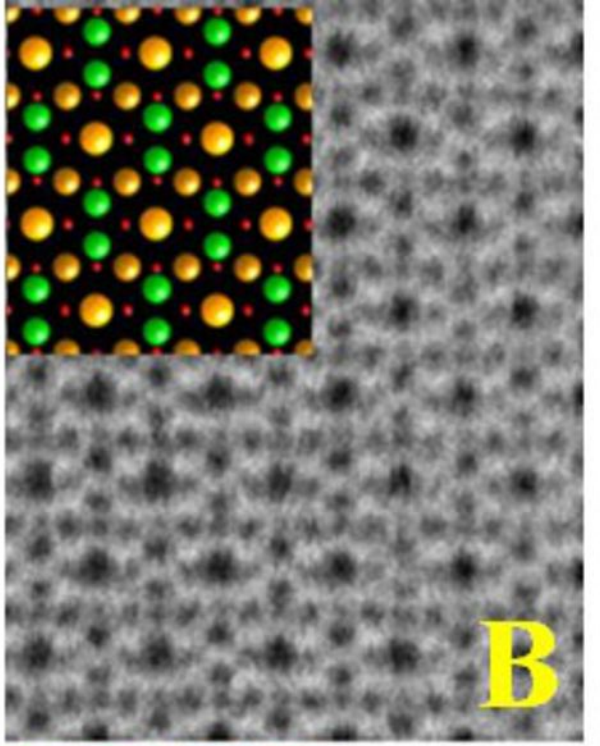
B

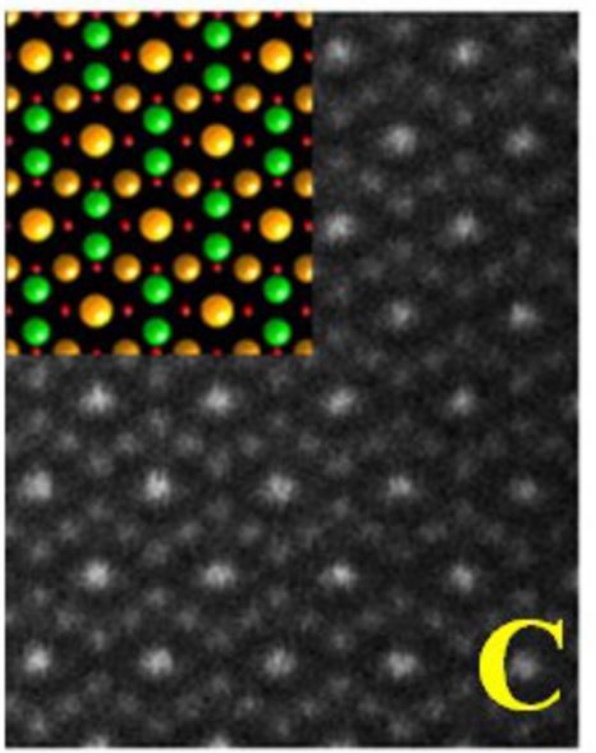
C

Fig. 2

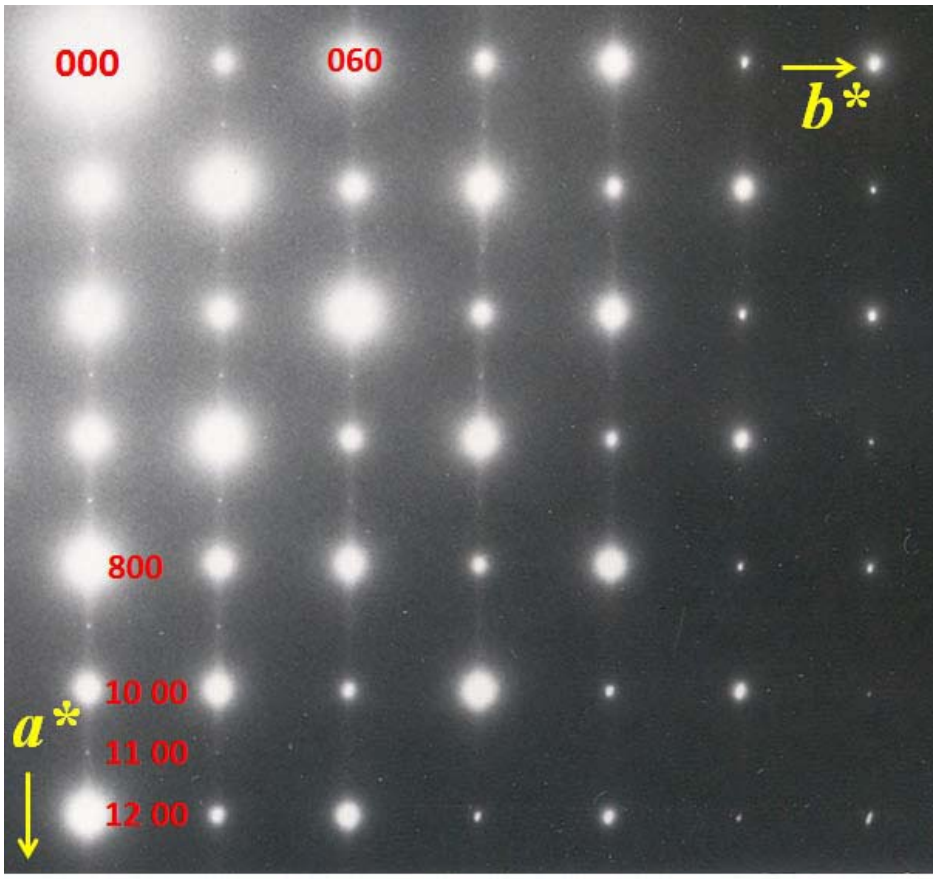

Fig. 3

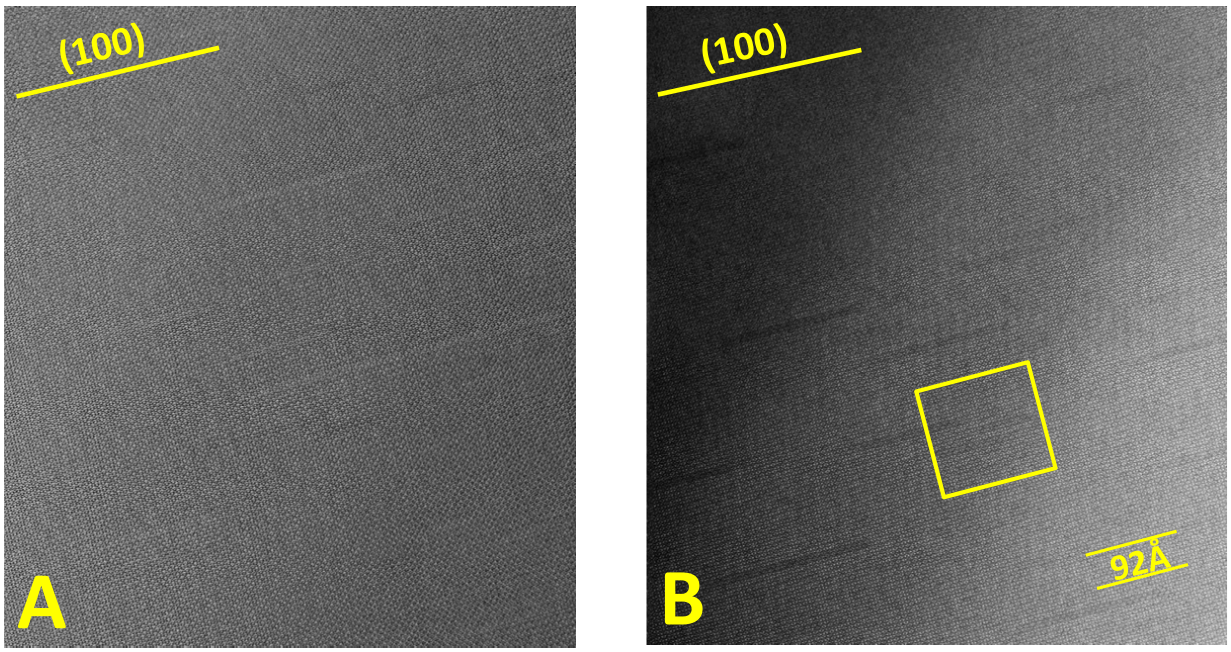

Fig. 4

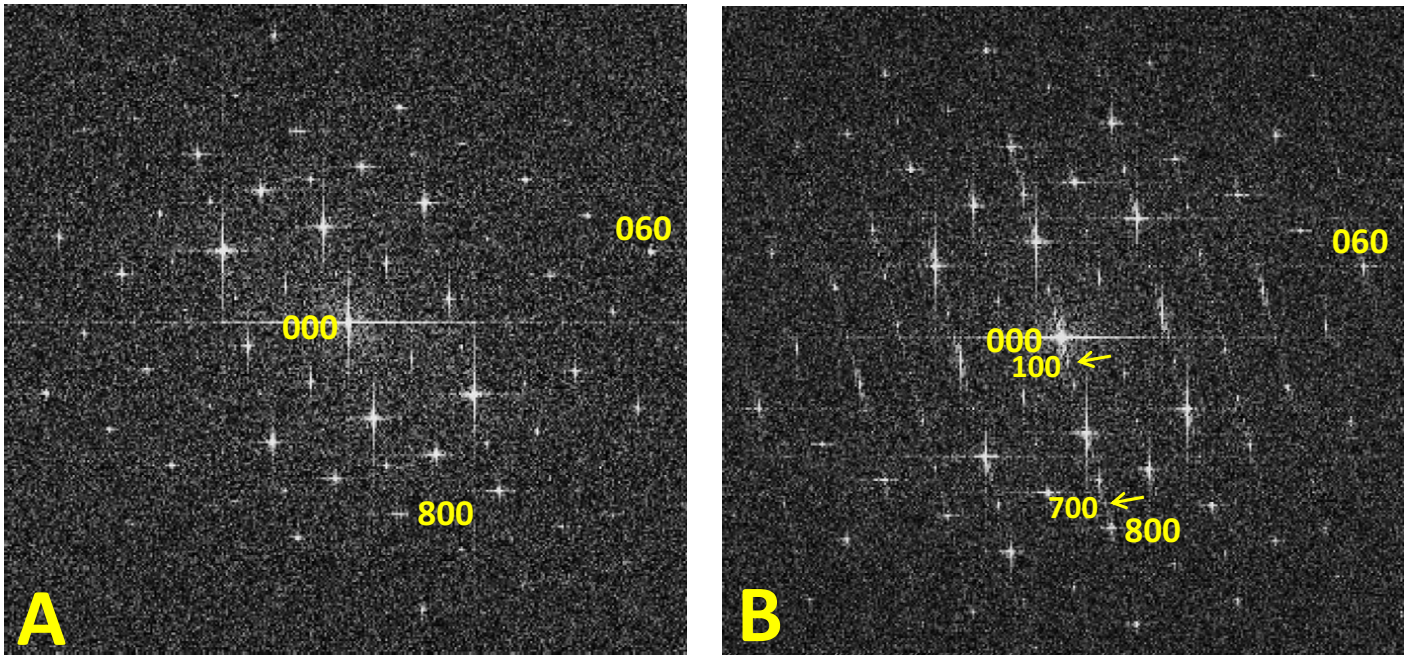

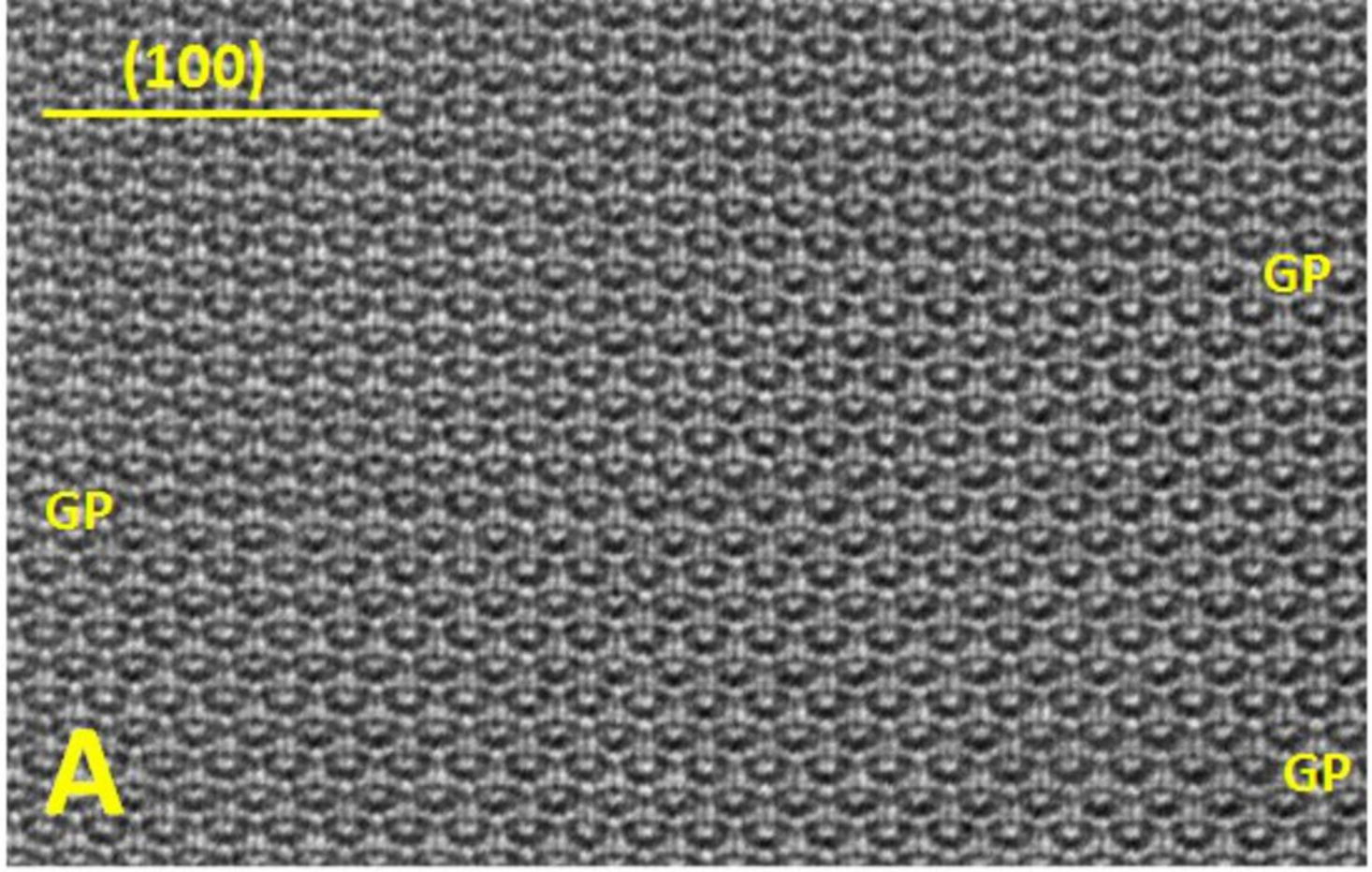
(100)
GP
GP
GP
A

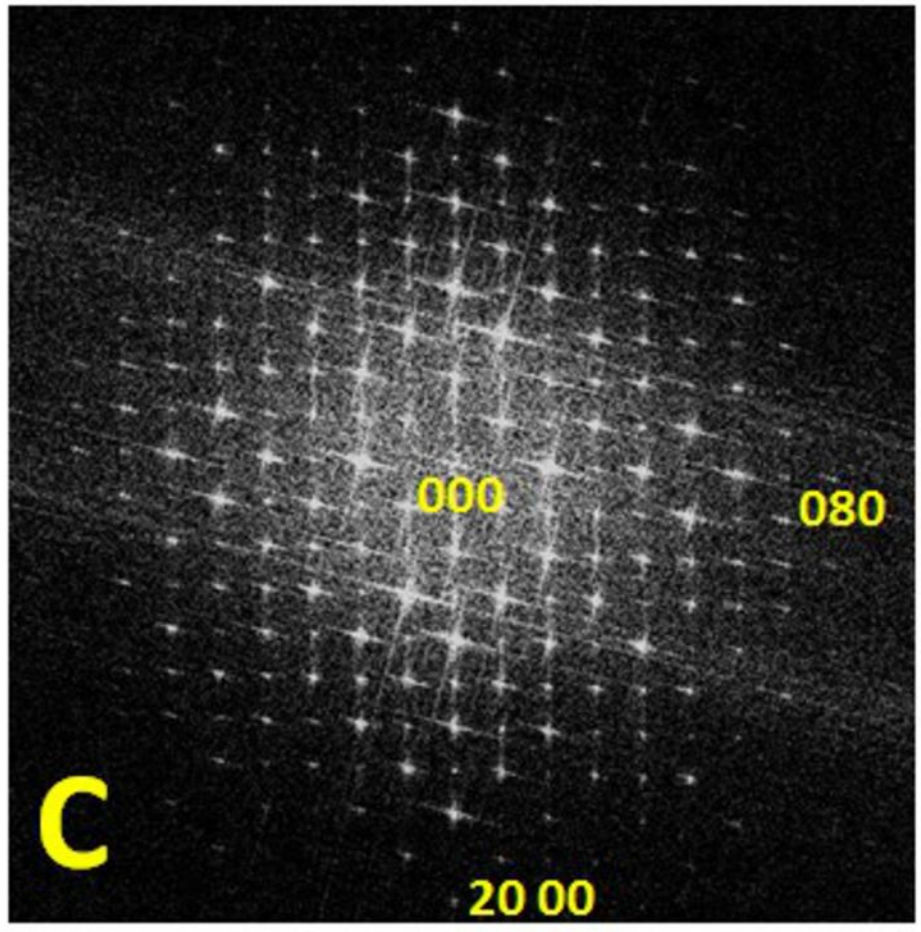
000
080
C
20 00

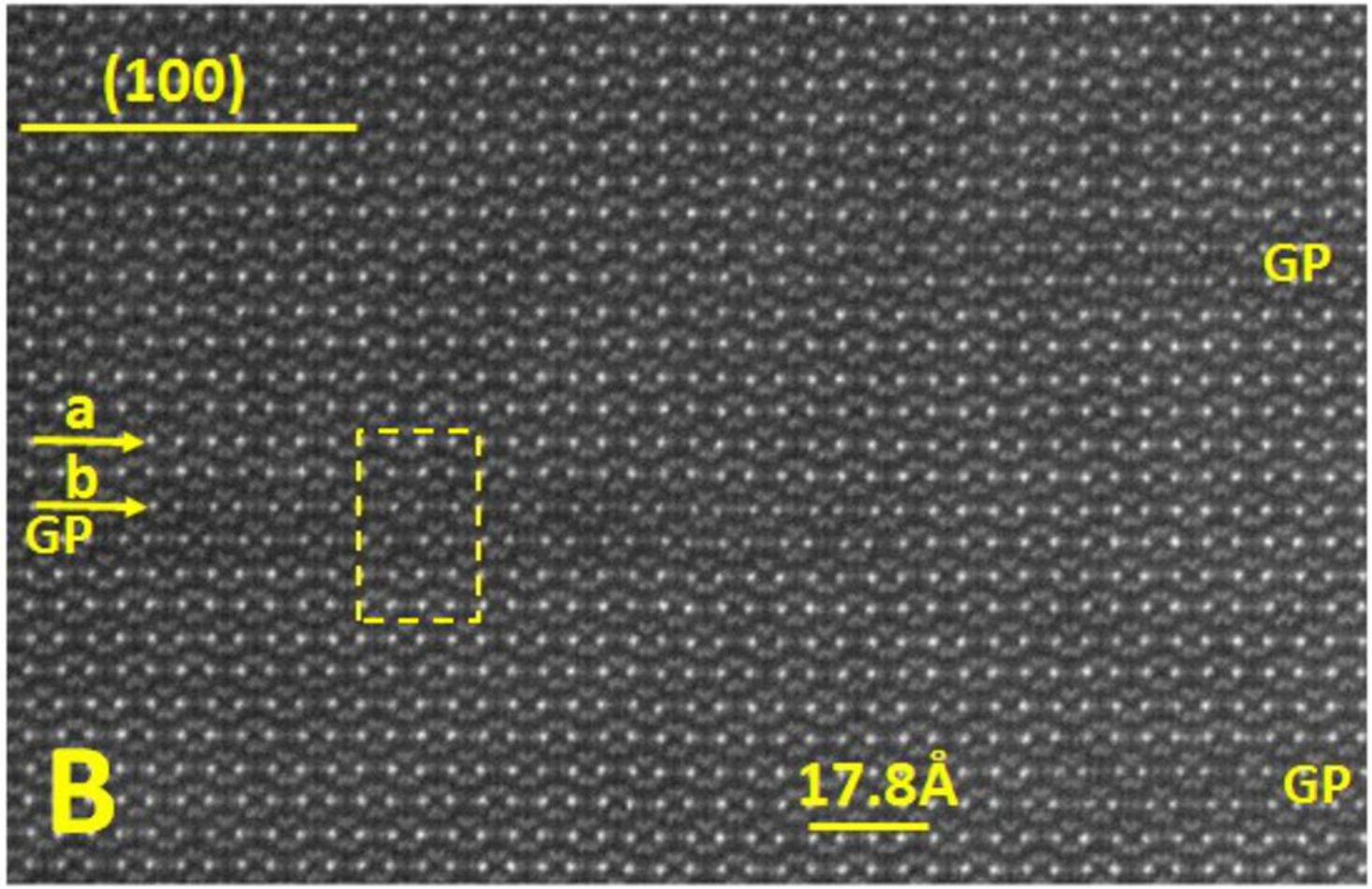
(100)
GP
a
b
GP
B
17.8Å
GP

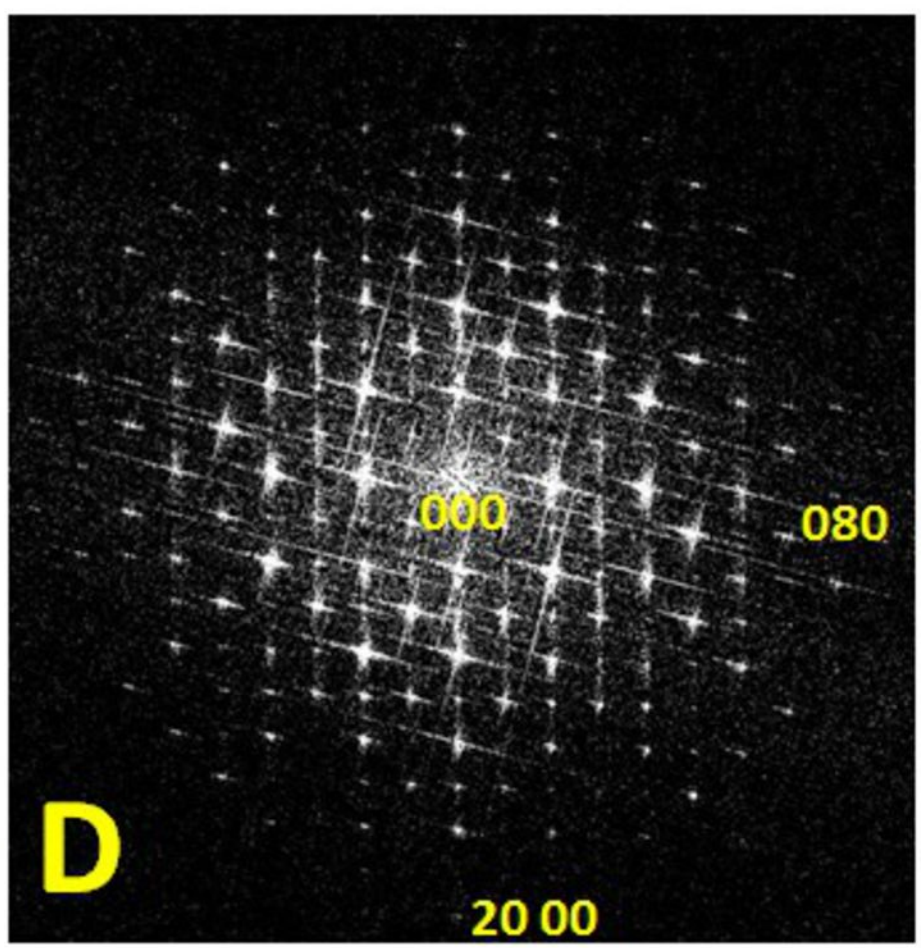
000
080
D
20 00

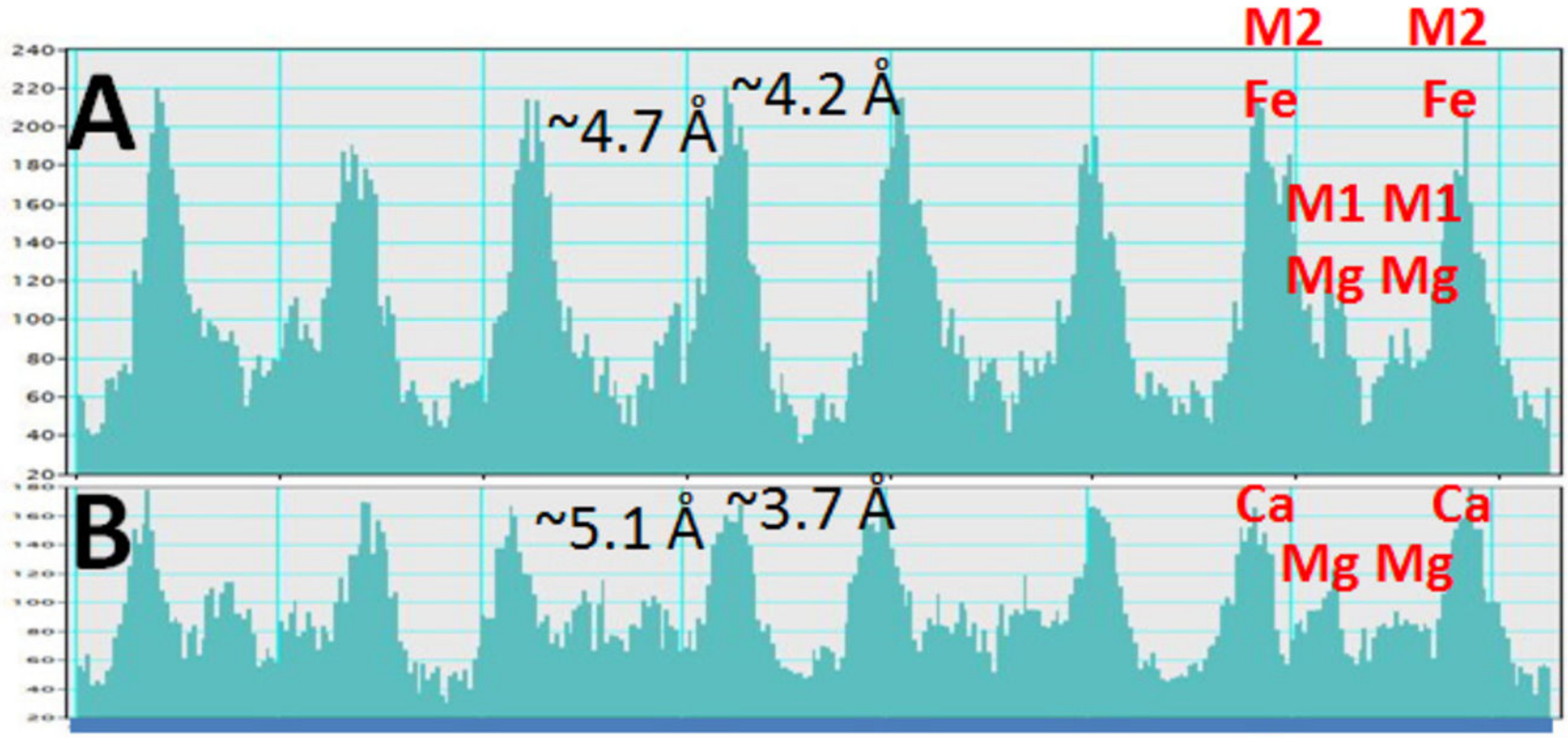

35 Å, along *b*-axis

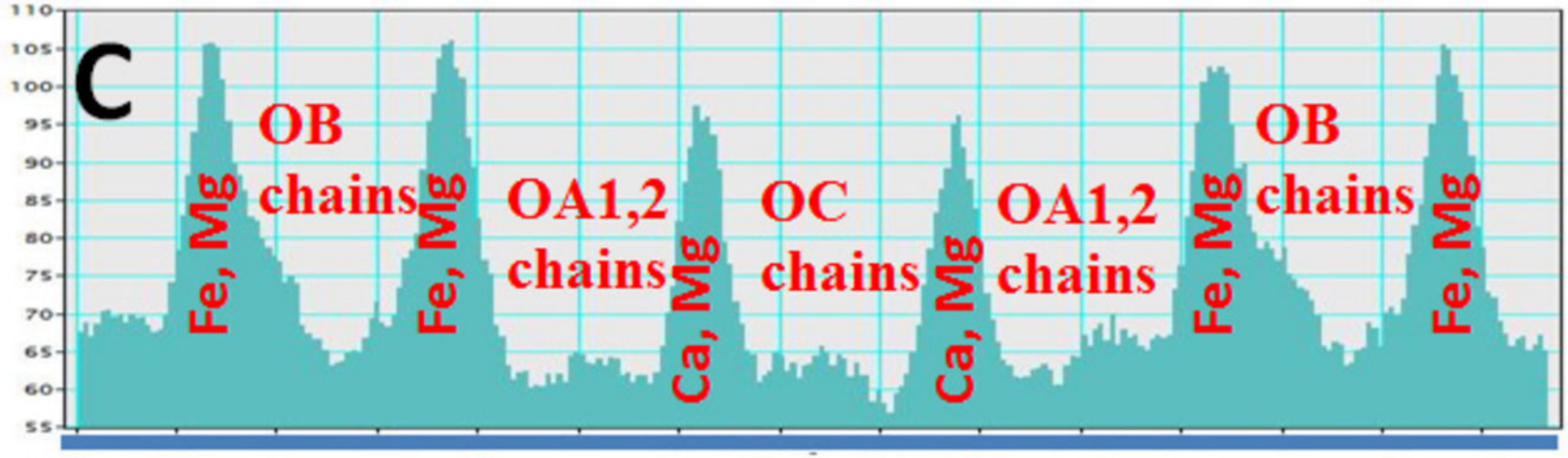

28 Å, along *a*-axis

(100)

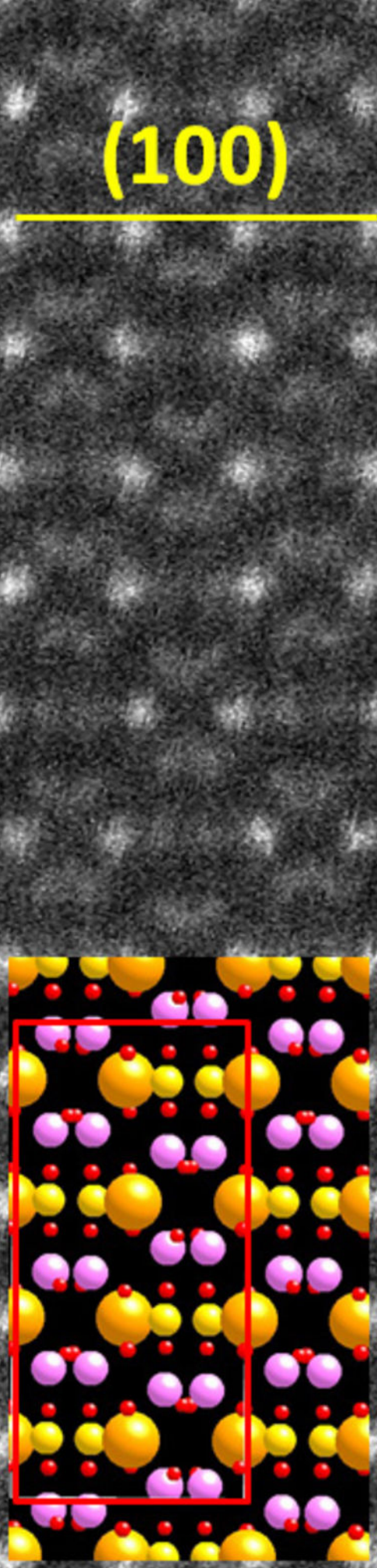

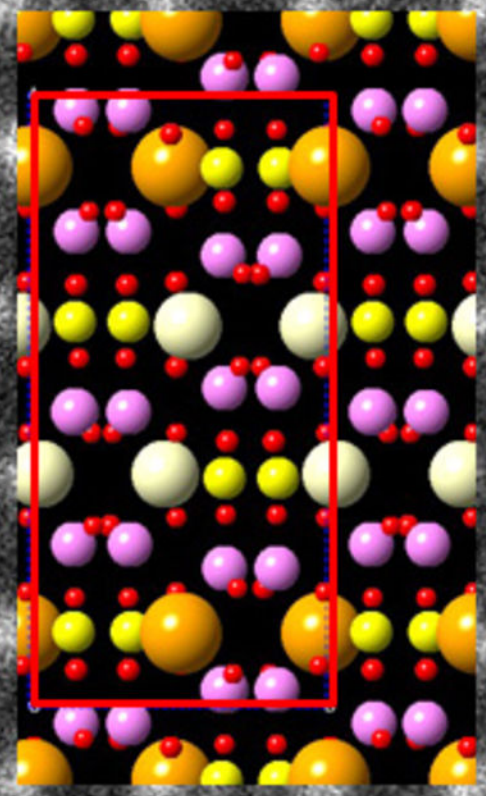

Fig. 8

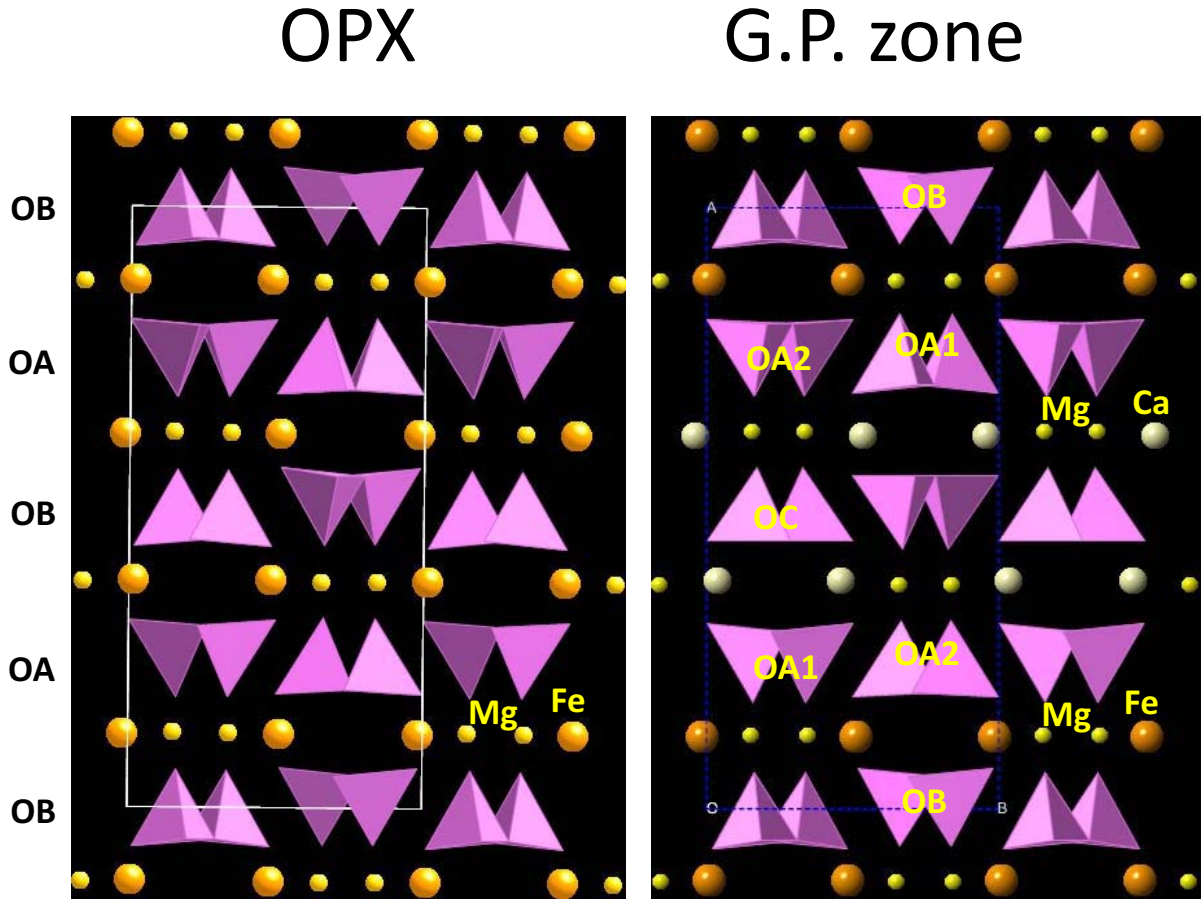

Fig. 9

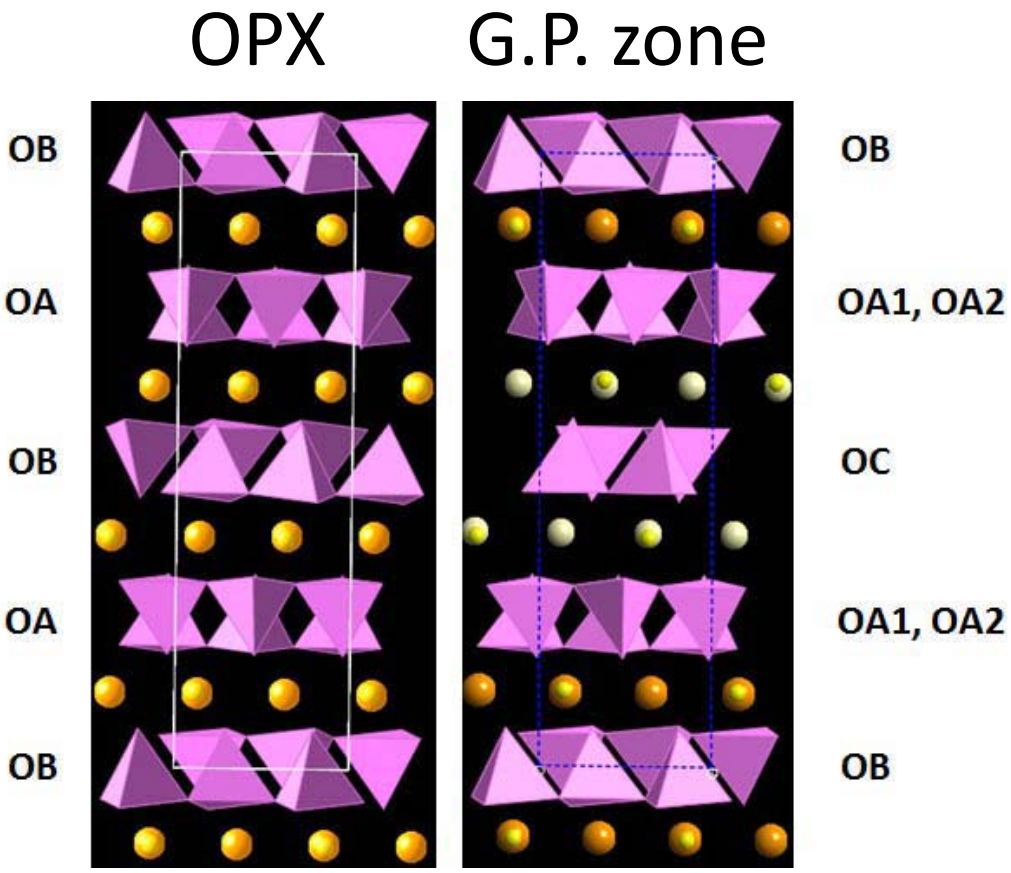

Fig. 10

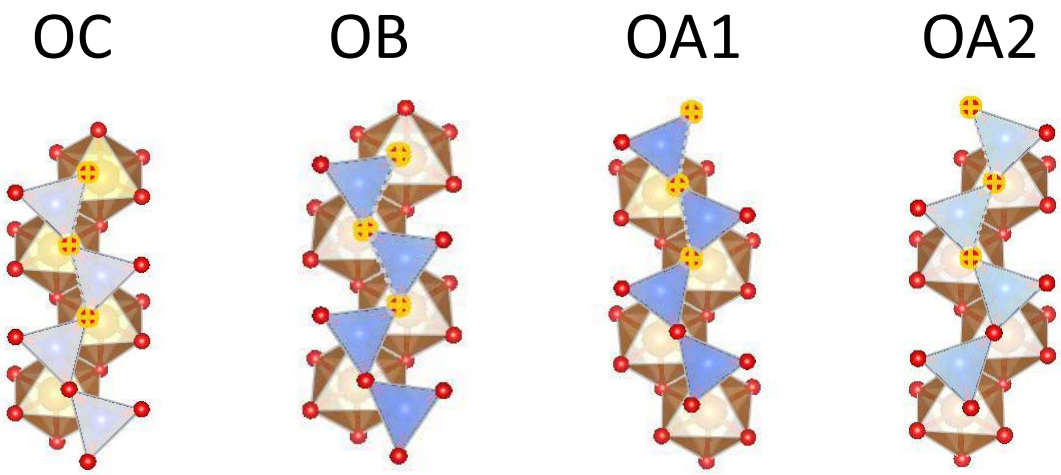

Fig. 11

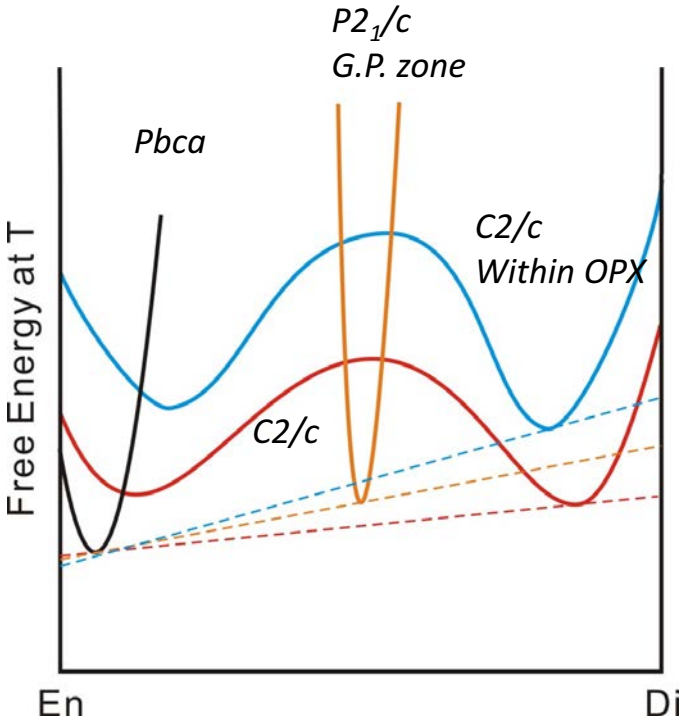

Table 1: Coordinates of atoms in a multi-layer G. P. zone structure with $P2_1/c$ symmetry.

Atom	x	y	z	Atom	x	y	z
Mg1A	0.1213	0.1526	0.8560	Mg2A	0.1190	0.5123	0.8483
Mg1B	0.3719	0.6591	0.8708	Ca2B	0.3788	0.0377	0.8744
Si1	0.2644	0.1556	0.5240	Si2	0.2245	0.6614	0.5609
Si3	0.4796	0.1592	0.3122	Si4	0.0277	0.6635	0.3073
O1	0.1767	0.1599	0.5173	O2	0.3124	0.6652	0.5403
O3	0.0607	0.1617	0.1902	O4	0.4330	0.6713	0.1968
O5	0.3073	0.0013	0.5089	O6	0.1856	0.5017	0.5283
O7	0.4455	0.0008	0.2358	O8	0.0662	0.5193	0.1848
O9	0.2936	0.2221	0.8044	O10	0.1935	0.7055	0.8577
O11	0.4463	0.2131	0.5975	O12	0.0531	0.6877	0.6172

Enstatite/diopside G. P. zone: $CaMg_3(Si_2O_6)_2$, Z = 4.

Table 2: Unit cell parameters of G. P. zone precipitate, enstatite, and diopside.

Lattice parameters	Enstatite		Diopside		G. P. zone	
	Calculated	Measured [a]	Calculated	Measured [b]	Calculated	Measured [c]
a (Å)	18.188	18.280	9.700	9.745	18.403	18.40
b (Å)	8.858	8.834	8.929	8.899	8.909	8.83
c (Å)	5.096	5.197	5.182	5.251	5.177	5.18
V ($Å^3$)	821.066	839.240	434.578	438.532	848.620	841.61
β (°)	90	90	104.46	105.63	90.53	90.0
E (eV)	-575.169		-294.351		-579.003	

[a] Carlson et al., 1988; [b] Cameron et al., 1973; [c] Smyth and Swope, 1990. Uncertainties for the measured unit-cell parameters of the host enstatite are ±0.006 Å, ±0.002 Å, and ±0.001 Å, along a- b- and c-axis respectively (Smyth and Swope, 1990). The uncertainties for the measured cell parameters of G.P. zone should be larger than those for the host crystal because of weak and diffuse reflections from the G.P. zones.